Supporting information

Thermally Tuning FeCoNiCrMn High-Entropy Alloy in Carbon Nanofibers for Superior Bifunctional Oxygen Electrocatalysis toward Flexible Zinc-Air Batteries

Lingli Xia [a, b], Peng Dai [a, *], Kun Huang [a], Hui Zhang [a], Zhenmeng Peng [c], Mingzai Wu [a, *]

[a] School of Materials Science and Engineering, Anhui University, Hefei, Anhui 230601, China.

[b] Army Arms University of PLA, Hefei, Anhui 230031, China.

[c] Department of Chemical and Biomolecular Engineering, University of Akron, Akron, OH 44325, USA.

[*] Corresponding authors.

E-mail addresses: daipeng@ahu.edu.cn (P. Dai), wumz@ahu.edu.cn (M. Wu).

1 Experimental Section

1.1 Materials

Chromic Chloride Hexahydrate (98%), Manganese acetate (99%), Cobaltous nitrate hexahydrate (99%), Nickel nitrate hexahydrate (98%), Ferric nitrate nonahydrate (98%), Ethanol absolute (99.7%), Acrylamide (99%), polyacrylonitrile, Potassium hydroxide (95%), isopropanol (99.7%) and Ammonium persulphate (98.5%) were bought from aladdin. Nafion solution (5wt%) were supplied by Du Pont. Acrylic acid, N, N'-methylenebis and N, N, N', N'-Tetramethylethylenediamine were supplied by Macklin. Deionized (DI) water (≥18.2 MΩ/cm) was purified by an ultra-pure purification system (Aqua Solutions).

1.2 Synthesis of the FeCoNiCrMn HEA nanoparticles supported on CNF

For a typical synthesis of the composite of carbon nanofibers, 0.1 mmol cobalt nitrate hexahydrate, nickel nitrate hexahydrate, iron nitrate nonahydrate, chromium trichloride hexahydrate, manganese acetate and 1.5 g polyacrylonitrile were dissolved in 20 mL N, N-Dimethylformamide with even stir for 2 h at room temperature. After that, the FeCoNiCrMn salts/PAN nanofibrous membranes were obtained through the electrospinning method. The electrospinning parameters were set as high voltage 15~17 KV, a distance of 13 cm between the syringe and the collector and a receiver speed of 500 r/min with the temperature and the humidity 25°C and 30%, respectively. The flow rate and electrospinning period were 0.5 mL h^{-1} and 12 h, respectively. The obtained nanofiber membrane was pre-oxidized in a muffle furnace and heated to 250°C at a heating rate of 2°C/min for 3 hours. Calcined in argon atmosphere for 3 hours. After natural cooling to room temperature, the FeCoNiCrMn/CNFs was obtained. Here, we chose 700°C to 900°C as the different setting temperatures.

1.3 Material characterization

A scanning electron microscope (SEM) images were obtained by Zeiss Auriga field emission scanning electron microscope. Transmission electron microscopy (TEM) images were obtained using a Tecnai F20 field emission gun microscope at a voltage of 200 kV with a point-to-point resolution of 0.19 nm. Image analysis was performed using Gatan Digital Micrograph software.

High angle annular dark-field (HAADF)-scanning transmission electron microscopy (STEM) images and elemental mapping were measured in a spherical aberration-corrected transmission electron microscope FEI Titan G2 80-200 ChemiSTEM with four energy-dispersive X-ray spectroscopy (EDX) detectors and operated at 80 and 200 keV. The crystal structure was characterized by powder X-ray diffraction (XRD) using the Rigaku smart Lab X-ray diffractometer. (Cu-Kα radiation, λ =1.5418 Å, 40 kV and 100 mA; Rigaku, Japan). Inductively coupled plasma-optical emission spectroscopy (ICP-OES) was conducted on an ICPE-9820 system. X-ray photoelectron spectroscopy (XPS) analysis using the ESCALAB 250 Xi X-ray photoelectron spectrometer. In-situ Raman spectra were collected using a Raman microscope (iHR320 monochromator, HORIBA) equipped with an in situ Raman cell (model: EC-RAIR-H, BJSCISTAR). The cell was made of polyetheretherketone (PEEK) and featured a platinum wire counter electrode and an Ag/AgCl reference electrode. The excitation source was a frequency-doubled Nd:YAG laser with an emission wavelength of 532 nm, and spectral acquisition was performed using a grating of 1800 lines/mm. Firstly, a 5-minute chronoamperometric measurement was conducted on the electrode at a specific applied voltage ranging from 1.1 to 1.6 V vs. RHE. Subsequently, Raman spectra were collected while the chronoamperometric measurement was maintained continuously. The pass energy was typically set to 100 eV for acquiring full spectra and to 30 eV for high-resolution elemental spectra.

1.4 Electrochemical measurements

All electrochemical measurements were performed at room temperature on a Chi760E electrochemical workstation (Shanghai Chenhua, China). A cut nanofiber membrane with an area of 1cm^2 was used as the working electrode, a platinum sheet was used as the counter electrode, and an Ag/AgCl electrode was used as the reference electrode. The electrode (Pt/C, RuO_2) was prepared as follows: 5 mg catalyst powder was weighed into 1 mL centrifuge tube, and 250 μL deionized water, 250 μL ethanol and 15 μL 5 wt % Nafion solution were added in turn. The mixture was ultrasonically treated for 1 h to form a uniform black catalyst ink. Subsequently, 8 μL of the ink was dropped onto the center of the rotating disk electrode (RDE)

to obtain a working electrode with a catalyst loading of 0.39 mg cm^{-2} and dried at room temperature. The as-prepared self-supported carbon nanofiber membrane was cut into 1 cm^2 pieces and directly used as the working electrode without any binder. In contrast, commercial Pt/C and RuO_2 catalysts were applied onto the substrate via the droplet coating method. For all samples, the catalyst mass loading was consistently maintained at 0.39 mg cm^{-2} to enable a fair comparison. It is important to note that the integrated self-supported electrode and the powder-coated electrode differ inherently in electrode morphology, mass transport behavior, and interfacial contact, due to the binder-free design. This limitation has been explicitly acknowledged in the current study, and a more standardized electrode configuration will be pursued in future work. All measured potentials ($E_{Ag/AgCl}$) were converted to the reversible hydrogen electrode (RHE) potential through the Nernst equation ($E_{RHE} = E_{Ag/AgCl} + 0.059 \times pH + E^{\theta}_{Ag/AgCl}$). Additionally, automatic positive feedback iR compensation was applied. The solution resistance was measured using electrochemical impedance spectroscopy (EIS) at the open-circuit potential over a frequency range of 100 kHz to 0.1 Hz with an AC amplitude of 5 mV. All linear sweep voltammetry (LSV) and cyclic voltammetry (CV) curves were recorded with 90% iR compensation, and no obvious oscillation was observed.

The oxygen evolution reaction (OER) measurements were performed in 0.1 M KOH electrolyte. The scan rate measured by linear sweep voltammetry (LSV) is 5 mV/s. Electrochemical impedance spectroscopy (EIS) measurements were recorded at AC voltages of 0.01-105 Hz.

The oxygen reduction reaction (ORR) measurements were performed in 0.1 M KOH electrolyte. The cyclic voltammetry (CV) curve was measured in 0.1 M KOH solution saturated with oxygen or argon at a scan rate of 10 mV/s. The linear sweep voltammetry (LSV) curve was carried out in an oxygen-saturated electrolyte. The rotation speed varied from 400 to 2500 rpm, and the scanning rate was also 10 mV/s.

The electron transfer number (n) was determined by the Koutecky-Levich equation:

$$\frac{1}{J} = \frac{1}{J_K} + \frac{1}{J_L} = \frac{1}{J_K} + \frac{1}{B\omega^{\frac{1}{2}}}$$

$$B = 0.62nFC_0D_0^{\frac{2}{3}}V^{-\frac{1}{6}}$$

where J is the measured current density, J_L is the limiting current density, J_K is the kinetic current density, n is the electron transfer number, ω is the angular velocity of the disk, F is the Faraday constant (96485 C mol^{-1}), C_0 is the bulk concentration of O_2 in 0.1 M KOH (1.2×10^{-6} mol cm^{-3}), D_0 is the diffusion coefficient of O_2 in 0.1 M KOH (1.9×10^{-5} cm^2 s^{-1}), V is the kinematic viscosity of the electrolyte (0.01 cm^2 s^{-1}).

1.5 Density functional theory (DFT) calculations

All density functional theory (DFT) calculations were performed using the Vienna Ab-initio Simulation Package (VASP).[1] The exchange-correlation effects were described by the Perdew-Burke-Ernzerhof (PBE) functional within the generalized gradient approximation (GGA).[2, 3] The core-valence interactions were treated using the projected augmented wave (PAW) method.[4] A plane-wave cutoff energy of 480 eV was employed, and the Brillouin zone was sampled using a 3×3×1 Monkhorst-Pack k-point grid. A vacuum layer of 15 Å was introduced above the surfaces to avoid periodic interactions. Structural optimizations were performed with energy and force convergence criteria set to 1.0×10^{-4} eV and 0.02 eV·$Å^{-1}$, respectively.

The adsorption energy can be calculated using the following formula:

$$Eads = E(A+B) - E(A) - E(B)$$

Where Eads represents the adsorption energy, E(A+B) denotes the calculated energy of the adsorption configuration, and E(A) and E(B) refer to the calculated energies of the substrate and adsorbent, respectively.

1.6 Zinc-air batteries (ZAB) measurements

Flexible zinc-air batteries (ZABs) were assembled using the obtained self-supporting composite film composed of carbon nanofibers and FeCoNiCrMn/CNFs-800 particles (catalyst loading: 0.5 mg cm^{-2}) as the air cathode, polished zinc foil as the anode, and our previously reported PAM-co-PAA gel as the electrolyte. Additionally, the flexible zinc-air battery was sealed with breathable and waterproof medical tape (Cofoe).The preparation of PAM-co-PAA

gel can be found in ref.[5] The PAM-co-PAA gel was prepared as follows: First, 9.0 g acrylamide (AM), 10 mL acrylic acid (AA), 0.1 g N, N'-methylenebis (acrylamide) (BIS) as cross-linker, and 0.1 mL N, N, N', N'-Tetramethylethylenediamine (TEMED) as accelerator were dissolved in 100 mL deionized water. Subsequently, 0.02 g initiator (ammonium persulfate) was added with rapid stirring for 10 s. The resulting solution was poured into a glass mold. After heating at 60°C for 2 h, the PAM-co-PAA hydrogel was obtained. Following a dehydration treatment (80°C for 12 h) and soaking in a 6 M KOH/0.2 M $Zn(CH_2COO)_2$ alkaline solution for 24 h, the PAM-co-PAA alkaline hydrogel electrolyte was obtained.

The charge-discharge polarization curves and open circuit voltage were measured by electrochemical workstation (Chi760E, Chenhua). The constant current test was carried out at room temperature using the LAND battery test system.

The specific capacity was calculated according to the following formula:

$$\text{specific capacity} = \frac{\text{current} \times \text{discharge time}}{\text{weight of consumed zinc}}$$

The energy density was calculated according to the following formula:

$$\text{energy density} = \frac{\text{current} \times \text{discharge time} \times \text{average discharge voltage}}{\text{weight of consumed zinc}}$$

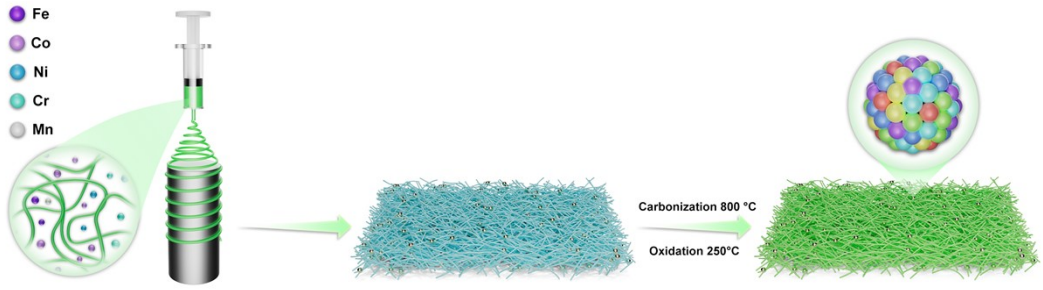

Fig. S1. Schematic diagram of the electrospinning synthesis process used to produce FeCoNiCrMn/CNFs-800.

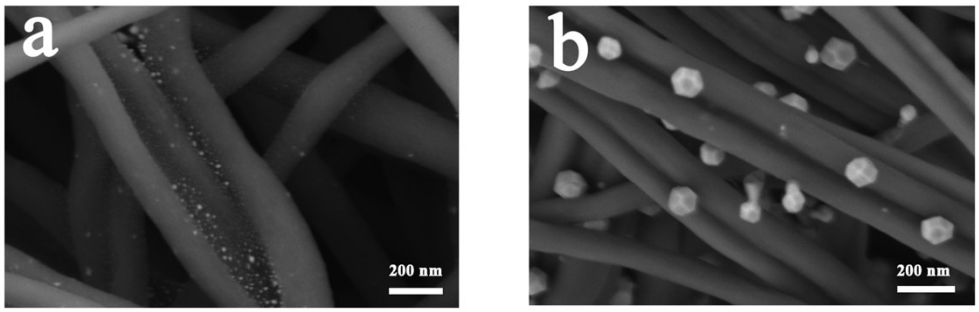

Fig. S2. SEM micrographs of FeCoNiCrMn/CNFs at different temperatures. (a) FeCoNiCrMn/CNFs-700. (b) FeCoNiCrMn/CNFs-900.

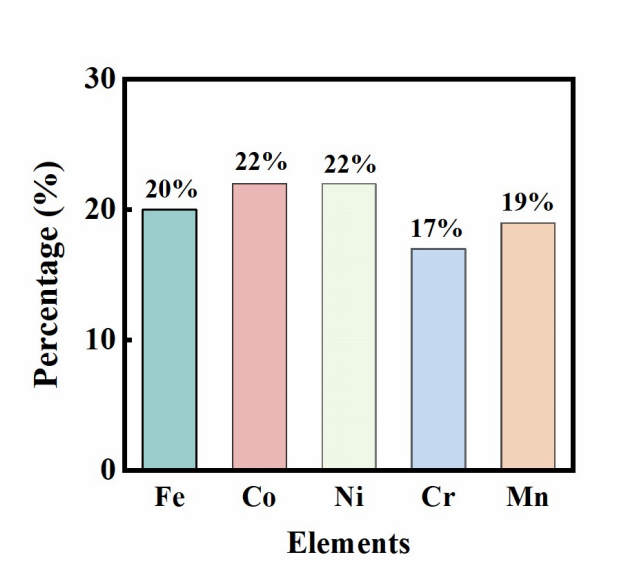

Fig. S3. ICP-OES composition of the FeCoNiCrMn/CNFs-800.

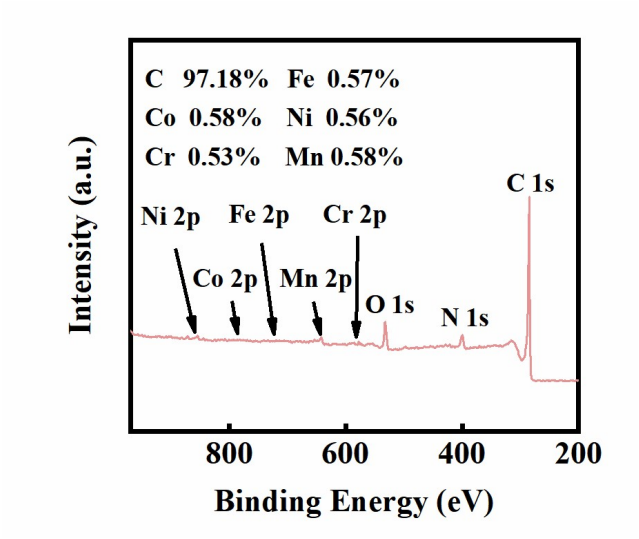

Fig. S4. The XPS survey spectrum of FeCoNiCrMn/CNFs-800.

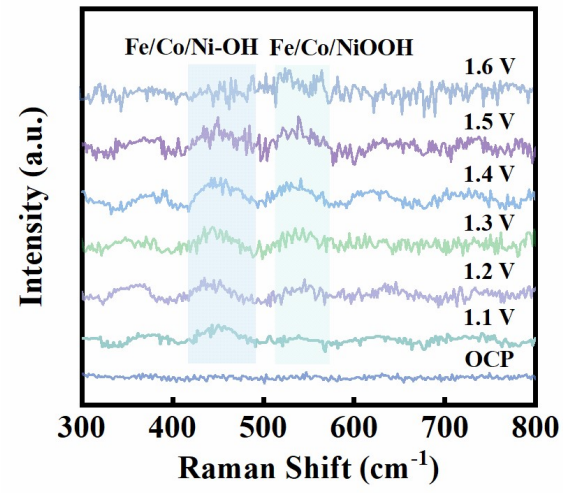

Fig. S5. In-situ Raman spectra of FeCoNiCrMn/CNFs-800 at different applied potentials.

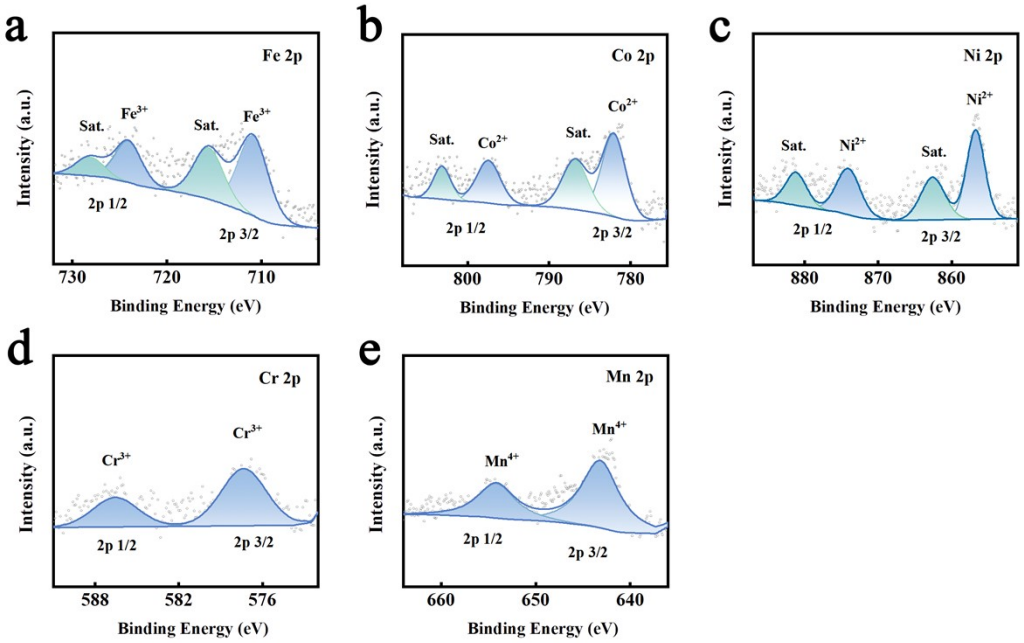

Fig. S6. High-resolution XPS spectra of FeCoNiCrMn/CNFs-800 after long-term OER measurements (a) Fe 2p, (b) Co 2p, (c) Ni 2p, (d) Cr 2p, (e) Mn 2p.

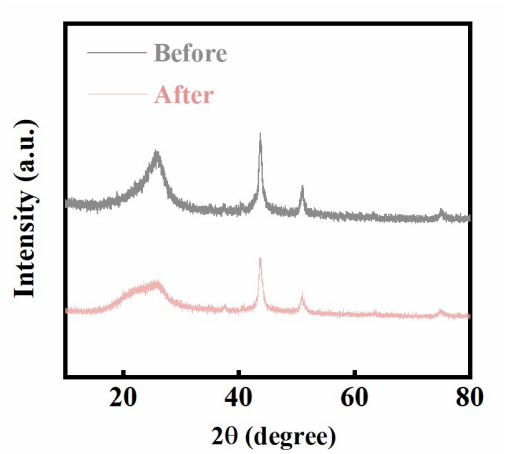

Fig. S7. XRD patterns of FeCoNiCrMn/CNFs-800 before and after OER stability measurement.

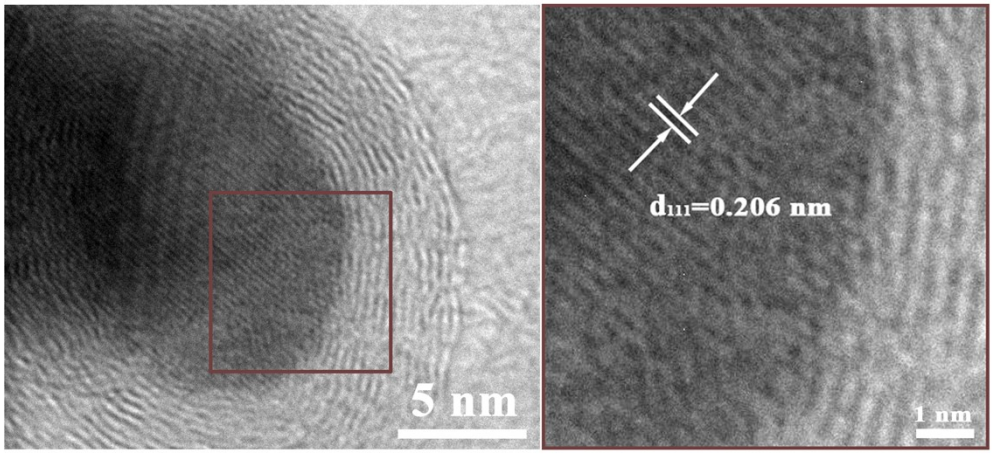

Fig. S8. HRTEM images of a FeCoNiCrMn/CNFs-800 after OER stability measurements. Enlarged HRTEM image of the red box area on the right.

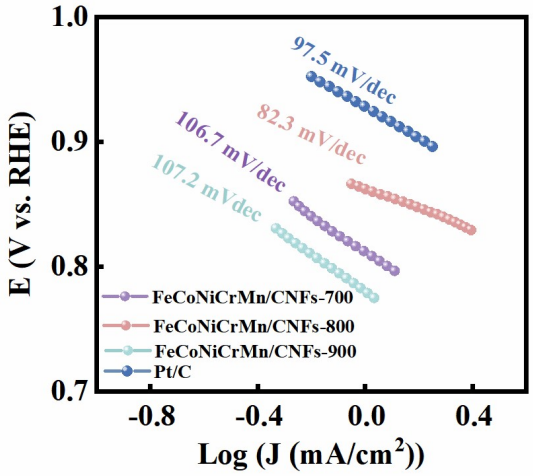

Fig. S9. Tafel slopes.

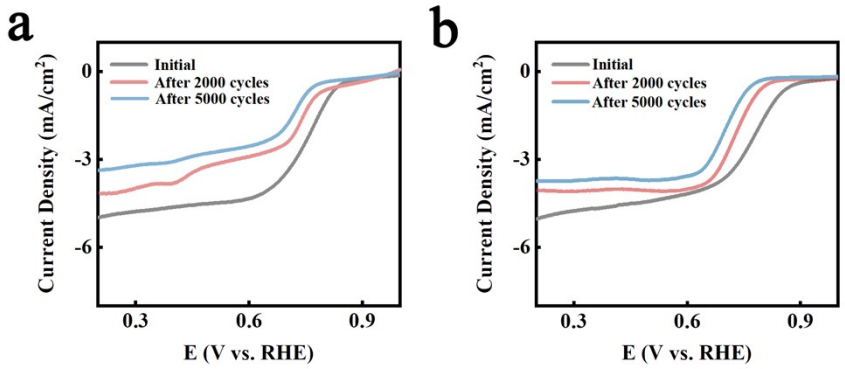

Fig. S10. (a) LSV curves before and after stability tests of 2000 and 5000 cycles of FeCoNiCrMn/CNFs-700. (b) LSV curves before and after stability tests of 2000 and 5000 cycles of FeCoNiCrMn/CNFs-900.

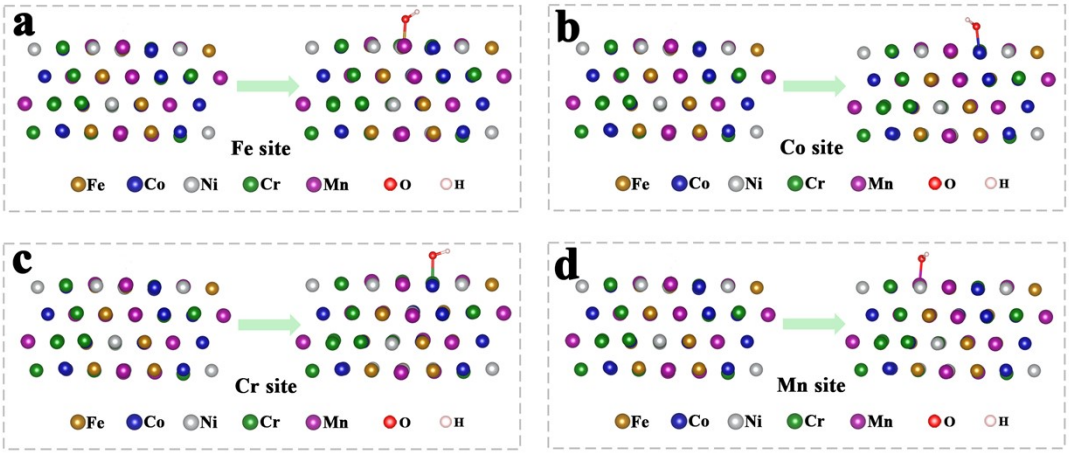

Fig. S11. The schematic diagram of the optimized structure of (a) Fe site, (b) Co site, (c) Cr site and (d) Mn site adsorbed OH* in FeCoNiCrMn/CNFs-800 during OER reaction.

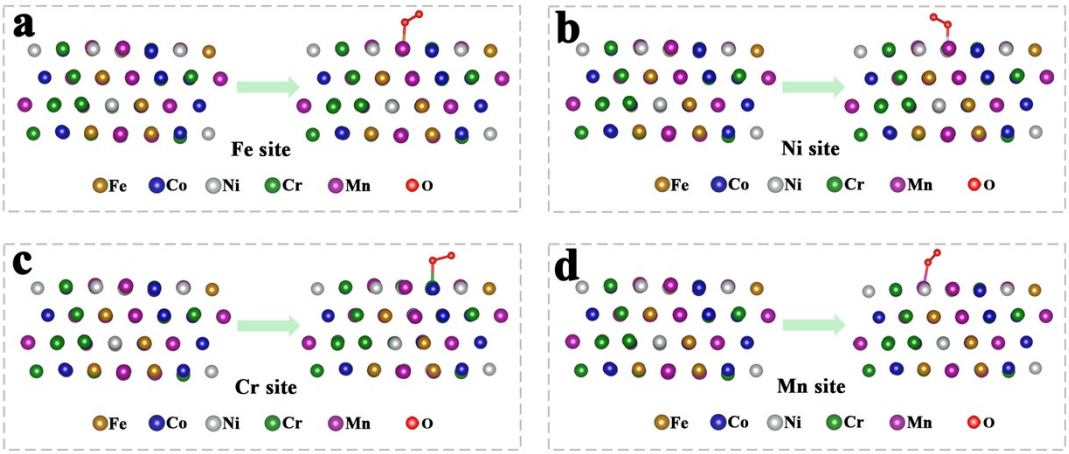

Fig. S12. The schematic diagram of the optimized structure of (a) Fe site, (b) Ni site, (c) Cr site and (d) Mn site adsorbed O_2 in FeCoNiCrMn/CNFs-800 during ORR reaction.

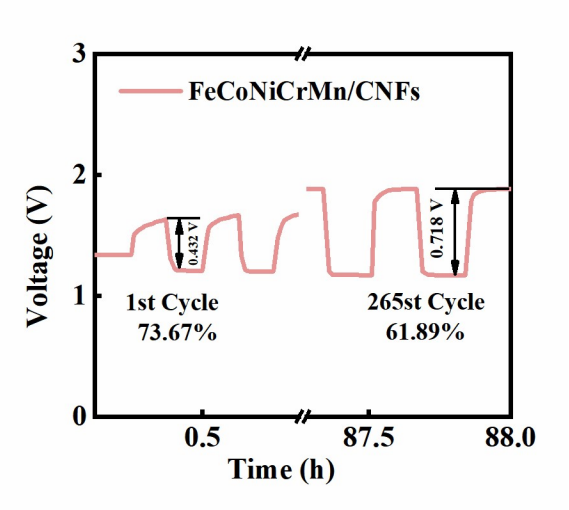

Fig. S13 The voltage efficiency of FeCoNiCrMn/CNFs-800-based flexible ZAB under different specific cycles.

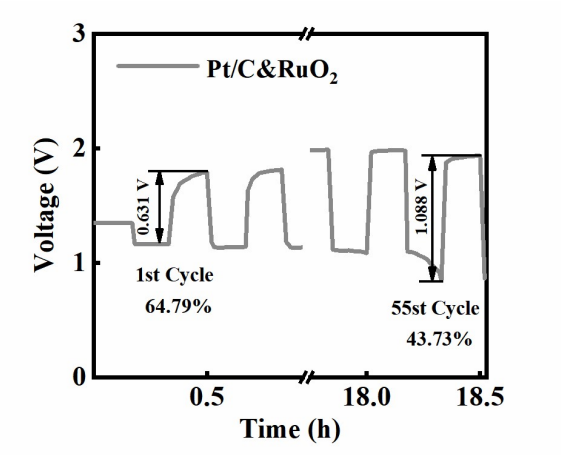

Fig. S14. The voltage efficiency of Pt/C&RuO_2 -based flexible ZAB under different specific cycles.

Table S1. OER performance comparison of FeCoNiCrMn/CNFs-800 with recently reported catalysts.

Catalyst	Substrate	Electrolyte	Overpotential@10 mA/cm^2 (mV)	Tafel slope (mV/dec)	References
FeMnCoCr	GCE	1M KOH	247	63	6
AlFeCoNiCr	GCE	1M KOH	270	52	7
$NiCo_2O_4$/Ni	CP	0.1M KOH	334	84	8
CoFeLaNiPt	GCE	0.1M KOH	377	150	9
NiS_2-rGO	GCE	1M KOH	370	59	10
CoFeGaNiZn	GCE	1M KOH	370	71	11
$FeNi_3$@NC	GCE	1M KOH	291	72.8	12
MnFeCoNi	CP	1M KOH	302	83.7	13
FeNi/N-C-800	GCE	0.1M KOH	370	128	14
$Mo_{0.6}Ni_{0.4}$	GCE	1M KOH	290	115	15
FeCoNiCrMn /CNFs-800	**CNM**	**0.1MKOH**	**230**	**49.3**	**This work**

CP: carbon paper; GCE: glassy carbon electrode; CNM: carbon nanofiber membrane.

Table S2. Comparison of the bifunctional activities of various state-of-the-art electrocatalysts for OER and ORR.

Catalyst	ORR $E_{1/2}$ (V vs. RHE)	OER $E_{j=10}$ (V vs. RHE)	$\Delta E = E_{j=10} - E_{1/2}$ (V)	References
NiS_2-rGO	0.76	1.52	0.76	16
AlFeCoNiCr	0.71	1.5	0.79	7
Co/Co_3O_4	0.83	1.505	0.675	17
FeCoNC/D	0.89	1.59	0.7	18
$FeNi_3$@NC	0.783	1.522	0.739	12
CoNi@NCNTs/CC	0.82	1.56	0.74	19
FeNi/N-C-800	0.845	1.6	0.755	14
Ce1-NG	0.869	1.611	0.742	20
NS-GR/Fe_3C	0.859	1.627	0.768	21
Co/N-PCM	0.83	1.564	0.734	22
Co_3O_4-x/NG	0.84	1.501	0.661	23
FeNi-NCS-2	0.867	1.625	0.758	24
FeNi@NC	0.85	1.521	0.671	25
Co-Fe	0.853	1.606	0.753	26
Pt/C	**0.82**	**1.85**	**1.03**	**This work**
RuO_2	**0.63**	**1.59**	**0.96**	**This work**
Pt/C&RuO_2	**0.82**	**1.59**	**0.77**	**This work**
FeCoNiCrMn/CNFs-800	**0.80**	**1.46**	**0.66**	**This work**

Table S3. Comparison of the performance of flexible ZAB obtained using the most advanced air cathode.

Catalyst	Open circuit potential (V)	Peak power density (mW/cm^2)	Cycling condition and stability (h)	References
γ -MnO_2/KC	1.36	62.4	2 mA/cm2, 10 h	27
CrMnFeCoNi	1.254	25.5	5 mA/cm^2, 50 h	28
IOSHs-NSC-Co_9S_8	1.408	60	5 mA/cm^2, 35 h	5
Co/MnO@N,S-C NT/CNFs	1.34	62.5	1 mA/cm^2, 15 h	29
AlFeCoNiCr	1.38	100	2 mA/cm^2, 60 h	7
Fe/Fe_3C@C-NCs	1.43	60	5 mA/cm^2, 40 h	30
ODAC-CoO	1.41	42	2 mA/cm^2, 12 h	31
Co/Co_3O_4	1.347	50.4	1 mA/cm2, 13.3 h	17
FeP/Fe_2O_3	1.42	40.8	5 mA/cm^2, 8.3 h	32
Ni-N_4/Co-O_4-MOF	1.38	78	5 mA/cm2, 40 h	33
Co-NCNT	1.45	144.6	5 mA/cm^2, 32 h	34
Fe_3C|Fe-N-C	1.414	63	5 mA/cm^2, 50 h	35
Co_2P/Co_3Fe_7	1.38	62.4	2 mA/cm^2, 62 h	36
Pt/C&RuO_2	**1.341**	**51**	**5 mA/cm^2, 18.5 h**	**This work**
FeCoNiCrMn/CNFs-800	**1.396**	**88**	**5 mA/cm^2, 88 h**	**This work**

References

1. G. Kresse and J. Hafner, *Physical Review B*, 1993, **47**, 558-561.
2. J. P. Perdew, K. Burke and M. Ernzerhof, *Physical Review Letters*, 1996, **77**, 3865-3868.
3. G. Kresse and D. Joubert, *Physical Review B*, 1999, **59**, 1758-1775.
4. P. E. Blöchl, *Physical Review B*, 1994, **50**, 17953-17979.
5. K. Tang, C. Yuan, Y. Xiong, H. Hu and M. Wu, *Applied Catalysis B: Environmental*, 2020, **260**, 118209.
6. P. Zhou, D. Liu, Y. Chen, M. Chen, Y. Liu, S. Chen, C. T. Kwok, Y. Tang, S. Wang and H. Pan, *Journal of Materials Science & Technology*, 2022, **109**, 267-275.
7. G. Fang, J. Gao, J. Lv, H. Jia, H. Li, W. Liu, G. Xie, Z. Chen, Y. Huang, Q. Yuan, X. Liu, X. Lin, S. Sun and H.-J. Qiu, *Applied Catalysis B: Environmental*, 2020, **268**, 118431.
8. P. Richtr, J. Hnát, J. Charvát, M. Bureš, J. Pocedič, M. Paidar, J. Kosek and P. Mazúr, *Journal of Energy Storage*, 2025, **115**, 115835.
9. M. W. Glasscott, A. D. Pendergast, S. Goines, A. R. Bishop, A. T. Hoang, C. Renault and J. E. Dick, *Nature Communications*, 2019, **10**, 2650.
10. K. Mathialagan, A. Thottungal, J. P. Richard, S. R. Pandimeenal, L. V. Nagaraj, S. T. Nishanthi and A. Bhaskar, *Materials Today Communications*, 2025, **49**, 114122.
11. L. Sharma, N. K. Katiyar, A. Parui, R. Das, R. Kumar, C. S. Tiwary, A. K. Singh, A. Halder and K. Biswas, *Nano Research*, 2022, **15**, 4799-4806.
12. X. Xie, H. Peng, K. Sun, X. Lei, R. Zhu, Z. Zhang, G. Ma and Z. Lei, *Chemical Engineering Journal*, 2023, **452**, 139253.
13. W. Dai, T. Lu and Y. Pan, *Journal of Power Sources*, 2019, **430**, 104-111.
14. Q. Xiong, J. Zheng, B. Liu, Y. Liu, H. Li and M. Yang, *Applied Catalysis B: Environmental*, 2023, **321**, 122067.
15. T. Zhang, X. Liu, X. Cui, M. Chen, S. Liu and B. Geng, *Advanced Materials Interfaces*, 2018, **5**, 1800359.
16. J. Li, S. Kang, H. Zhang, J. Yang, P. Wan, Z. Li, S. Wu, Y. Sun and Q. Yang, *Green Chemistry*, 2025, **27**, 10755-10766.
17. B. Zhang, T. Lu, Y. Ren, L. Huang, H. Pang, Q. Zhao, S. Tian, J. Yang, L. Xu, Y. Tang and X. Tian, *Chemical Engineering Journal*, 2022, **448**, 137709.
18. K. Kim, K. Min, Y. Go, Y. Lee, S. E. Shim, D. Lim and S.-H. Baeck, *Applied Catalysis B: Environmental*, 2022, **315**, 121501.
19. W.-W. Tian, J.-T. Ren and Z.-Y. Yuan, *Applied Catalysis B: Environmental*, 2022, **317**, 121764.
20. J. Sun, Z. Wang and J. Guan, *Materials Chemistry Frontiers*, 2025, **9**, 1574-1580.
21. K. Kohila Rani, C. Karuppiah, S.-F. Wang, S. O. Alaswad, P. Sireesha, R. Devasenathipathy, R. Jose and C.-C. Yang, *Ultrasonics Sonochemistry*, 2020, **66**, 105111.
22. F. Tang, Z. Wang, S. Wang, S. Xing, C. Li, S. Wang, Z. Jin and J.-B. Baek, *Chemical Engineering Journal*, 2024, **487**, 150433.
23. J. Qin, Z. Liu, D. Wu and J. Yang, *Applied Catalysis B: Environmental*, 2020, **278**, 119300.

24. Z. Yao, D. Chen, Y. Li, Q. Lyu, J. Wang and Q. Zhong, *International Journal of Hydrogen Energy*, 2022, **47**, 984-992.
25. S. Liu, K. Dong, X. Lei, K. Sun, X. Xie, H. Peng and G. Ma, *Journal of Energy Storage*, 2024, **89**, 111862.
26. Y. Lian, K. Shi, H. Yang, H. Sun, P. Qi, J. Ye, W. Wu, Z. Deng and Y. Peng, *Small*, 2020, **16**, 1907368.
27. D. Wang, J. Li, Q. Zhuang, J. Luo, G. Cheng, J. Huang, T. Xue, M. Sun, F. Ye and L. Yu, *Materials Today Energy*, 2025, **53**, 101975.
28. R. He, L. Yang, Y. Zhang, X. Wang, S. Lee, T. Zhang, L. Li, Z. Liang, J. Chen, J. Li, A. Ostovari Moghaddam, J. Llorca, M. Ibáñez, J. Arbiol, Y. Xu and A. Cabot, *Energy Storage Materials*, 2023, **58**, 287-298.
29. Q. Zhou, S. Hou, Y. Cheng, R. Sun, W. Shen, R. Tian, J. Yang, H. Pang, L. Xu, K. Huang and Y. Tang, *Applied Catalysis B: Environmental*, 2021, **295**, 120281.
30. Z. Cao, H. Hu, M. Wu, K. Tang and T. Jiang, *Journal of Materials Chemistry A*, 2019, **7**, 17581-17593.
31. Y. Tian, X. Liu, L. Xu, D. Yuan, Y. Dou, J. Qiu, H. Li, J. Ma, Y. Wang, D. Su and S. Zhang, *Advanced Functional Materials*, 2021, **31**, 2101239.
32. K. Wu, L. Zhang, Y. Yuan, L. Zhong, Z. Chen, X. Chi, H. Lu, Z. Chen, R. Zou, T. Li, C. Jiang, Y. Chen, X. Peng and J. Lu, *Advanced Materials*, 2020, **32**, 2002292.
33. W. Yan, Q. Tang, L. Liu, Y. Zhang, L. Shi, W. Chen and Y. Chen, *Journal of Energy Storage*, 2025, **118**, 116335.
34. Z. Pei, Y. Huang, Z. Tang, L. Ma, Z. Liu, Q. Xue, Z. Wang, H. Li, Y. Chen and C. Zhi, *Energy Storage Materials*, 2019, **20**, 234-242.
35. Y. Chen, X. Kong, Y. Wang, H. Ye, J. Gao, Y. Qiu, S. Wang, W. Zhao, Y. Wang, J. Zhou and Q. Yuan, *Chemical Engineering Journal*, 2023, **454**, 140512.
36. A. Feng, L. Liu, P. Liu, Y. Zu, F. Han, X. Li, S. Ding and Y. Chen, *Materials Today Energy*, 2024, **44**, 101626.